Journal of Membrane Science 734 (2025) 124437

Contents lists available at ScienceDirect

Journal of Membrane Science

journal homepage: www.elsevier.com/locate/memsci

Fabrication of highly *a*-oriented ultrathin FER zeolite membrane from nanosheets towards small-sized gas separation

Yi Liu [a], Weili Qiang [b], Jinming Lu [a], Yi Liu [a,c,*]

[a] State Key Laboratory of Fine Chemicals, Frontiers Science Center for Smart Materials, School of Chemical Engineering, Dalian University of Technology, Linggong Road 2, Ganjingzi District, Dalian, 116024, China
[b] School of Materials Science and Engineering, Dalian Jiaotong University, Dalian, 116028, China
[c] Dalian Key Laboratory of Membrane Materials and Membrane Processes, Dalian University of Technology, Linggong Road 2, Ganjingzi District, Dalian, 116024, China

ARTICLE INFO

Keywords:
Gas separation
Zeolite membrane
Nanosheets
Orientation
Helium separation

ABSTRACT

Although zeolites have attracted considerable interest due to their well-defined pore structure, excellent stability, and tailorable functionality, rational design and engineering of high-performance zeolite membranes for small-sized gas separation represents a grand challenge. In this study, we pioneered the preparation of highly *a*-oriented ultrathin FER zeolite membranes from uniform FER nanosheets with an unprecedented aspect ratio of ~180. Among various factors, fabrication of FER nanosheet seeds by dynamic hydrothermal crystallization and bulk nucleation inhibition during epitaxial growth were found crucial for obtaining FER membranes with desired microstructure. Benefiting from the vertical alignment of 0.28 nm-sized 6-membered ring pore apertures on porous α-Al_2O_3 substrate, the membrane exhibited superior selectivity towards small-sized gas molecules, such as He/CO_2 (19.5), He/N_2 (23.8) and He/CH_4 (26.6), showing great promise in high-efficiency helium recovery from natural gas.

1. Introduction

Helium, a noble gas with unique properties such as low boiling point, exceptional chemical inertness, and high thermal conductivity, represents the indispensable resource in diverse advanced technologies including medical imaging, semiconductor fabrication, and quantum computing [1–3]. This finite, non-renewable resource is predominantly extracted from natural gas deposits, where it typically constitutes less than 1 % of the gas mixture alongside methane (CH_4), nitrogen (N_2), and carbon dioxide (CO_2). Consequently, efficient extraction and purification processes are vital to satisfy its global demand and guarantee long-term availability [4–6].

Conventional helium recovery methods, such as cryogenic distillation and pressure swing adsorption, suffer from high energy consumption and operational complexity, driving the demand for developing high-efficiency separation technologies [7,8]. Membrane technology, with inherent advantages of low energy consumption, operational simplicity, and environmental friendliness, has emerged as a promising alternative [9–12]. Among the diverse membrane materials, polymer membranes represent the most technologically mature option for industrial gas separation, primarily due to their low cost and excellent processability into large-area modules [13,14]. Specifically for helium recovery from natural gas, glassy polymers like polyimides and polysulfones have been extensively investigated [15]. However, their separation performance is intrinsically constrained by the well-established trade-off between permeability and selectivity, a limitation delineated by the Robeson upper bound [16]. Consequently, even advanced polymeric membranes that achieve high He permeance often exhibit only modest He/CH_4 selectivity. Moreover, their long-term stability and performance are susceptible to degradation under aggressive feed conditions containing CO_2, moisture, and heavy hydrocarbons, which can induce detrimental plasticization or competitive sorption [17]. These persistent challenges underscore the critical need for advanced inorganic membranes. Inorganic materials, particularly zeolites, are compelling alternatives as they offer superior selectivity derived from their precise, molecular-sieving pore structures and exceptional thermal and chemical stability, providing an opportunity to overcome the inherent limitations of their polymeric counterparts [18–20].

This article is part of a special issue entitled: Early Career Membrane Scientists published in Journal of Membrane Science.

[*] Corresponding author. Dalian Key Laboratory of Membrane Materials and Membrane Processes, Dalian University of Technology, Linggong Road 2, Ganjingzi District, Dalian, 116024, China.

E-mail address: diligenliu@dlut.edu.cn (Y. Liu).

https://doi.org/10.1016/j.memsci.2025.124437
Received 17 May 2025; Received in revised form 3 July 2025; Accepted 10 July 2025

Ferrierite (FER)-type zeolites, exemplified by ZSM-35, feature a unique two-dimensional pore system comprising 10-membered ring (10-MR) channels (~4.2 × 5.4 Å) parallel to the *c*-axis and 8-MR channels (~3.5 × 4.8 Å) parallel to the *b*-axis, with 0.6–0.7 nm spherical FER cages forming at their intersections (Fig. S1) [21–23]. Although no straight-through channels exist along the *a*-crystallographic direction, molecular transport can proceed via a tortuous pathway facilitated by the 6-MR windows along *a*-axis that connect adjacent FER cages (Fig. S2). Given that 6-MR pore apertures in zeolites typically exhibit a maximum pore size of 0.28 nm [24,25], FER zeolite membrane with a pronounced *a*-out-of-plane orientation (i.e., 6-MR pores along the *a*-axis) is anticipated to create a highly selective pathway for preferential He (0.26 nm) permeation. This configuration is expected to exclude common natural gas components like CO_2 (0.33 nm), N_2 (0.36 nm) and CH_4 (0.38 nm), enabling ultrahigh perm-selectivity for He. Furthermore, reducing membrane thickness represents a reliable strategy for decreasing the diffusion barrier and enhancing He permeance [26,27]. Therefore, the development of highly *a*-oriented FER membranes with ultrathin thickness is attractive for achieving high-efficiency helium recovery.

Motivated by the above concerns, in this work, we pioneered the fabrication of highly *a*-oriented ultrathin FER zeolite membranes through nanosheet-seeded epitaxial growth. The procedure was briefly described as follow (Fig. 1): Initially, high-aspect-ratio FER nanosheet (NS) seeds were prepared through one-step dynamic hydrothermal crystallization. Subsequently, uniform seed layer was deposited on porous α-Al_2O_3 substrate via vacuum-assisted hot-drop coating. Finally, controlled in-plane epitaxial growth was conducted to obtain FER zeolite membrane with desired morphology. Owing to the intrinsic structural superiority derived from concurrent control of membrane orientation and thickness, the obtained FER membrane demonstrated excellent performance in helium containing small-sized gas separation.

2. Experimental section

2.1. Reagents and materials

LUDOX® AS-40 colloidal silica (SiO_2, 40 wt% suspension in H_2O, Sigma-Aldrich), aluminum sulfate octadecahydrate ($Al_2(SO_4)_3{\cdot}18H_2O$, 99.95 %, Macklin), sodium hydroxide (NaOH, 99.9 %, Macklin), potassium hydroxide (KOH, 99.99 %, Macklin), pyridine (C_5H_5N, 99.5 %, Macklin) were used as received without further purification. Porous α-Al_2O_3 disks with the diameter of 18 mm, thickness of 1 mm and pore size of 70 nm were acquired from Fraunhofer IKTS, Germany.

2.2. Preparation of FER zeolite NSs

FER zeolite NSs were synthesized from a precursor solution with molar composition of 12.5Na_2O: 5.5K_2O: 120SiO_2: 1Al_2O_3: 72C_5H_5N: 2400H_2O. In a typical experiment, 11.250 g of colloidal silica was added dropwise into a clearly basic solution containing 0.630 g of NaOH, 0.379 g of KOH and 20.048 g of DI (deionized) H_2O. After being aged under vigorous stirring at 50 °C for 2 h, 0.415 g of $Al_2(SO_4)_3{\cdot}18H_2O$ was added and stirred for another 2 h. Subsequently, 3.560 g of C_5H_5N was added and obtained mixture was aged under vigorous stirring at 50 °C for 1.5 h. The resultant gel was transferred into a 50 mL Teflon-lined stainless-steel autoclave and subjected to hydrothermal crystallization in a pre-heated rotational oven (20 r/min) at 160 °C for 72 h. Afterwards, solid products were separated by centrifugation, washed thoroughly with DI water and the wet solid product was freeze-dried for at least 24 h. As a comparative experiment, the crystallization was conducted under identical hydrothermal conditions except that a pre-heated static oven was employed.

2.3. Oriented deposition of FER seed layer

Prior to the seeding, asymmetric α-Al_2O_3 disks were pretreated with 6.0 vol% HCl solution, thoroughly rinsed with DI water, and finally air-dried overnight at 70 °C. The oriented FER seed layer was fabricated through vacuum-assisted hot-drop coating (Fig. S3). First, a homogeneous FER NS suspension (0.01 wt% in ethanol, Fig. S4) was prepared by dispersing freeze-dried FER NSs in ethanol under intensive sonication. Afterwards, porous α-Al_2O_3 substrate was pre-heated to 100 °C on a vacuum-compatible heating plate, followed by deposition of 0.2 mL suspension onto the substrate surface. Upon complete ethanol evaporation from the substrate-deposited suspension, the α-Al_2O_3 disk was carefully detached from the coating apparatus and placed in a convection oven at 100 °C to eliminate residual ethanol. Finally, obtained FER seed layer was heated in air at 500 °C for 1 h with controlled heating/cooling rate of 60 $°C{\cdot}min^{-1}$.

2.4. Preparation of oriented FER zeolite membrane

The precursor solution with molar composition of 12.5Na_2O: 5.5K_2O: 120SiO_2: 1Al_2O_3: 80C_5H_5N: 9600H_2O was prepared using identical synthetic protocols as FER zeolite NSs. In a typical experiment,

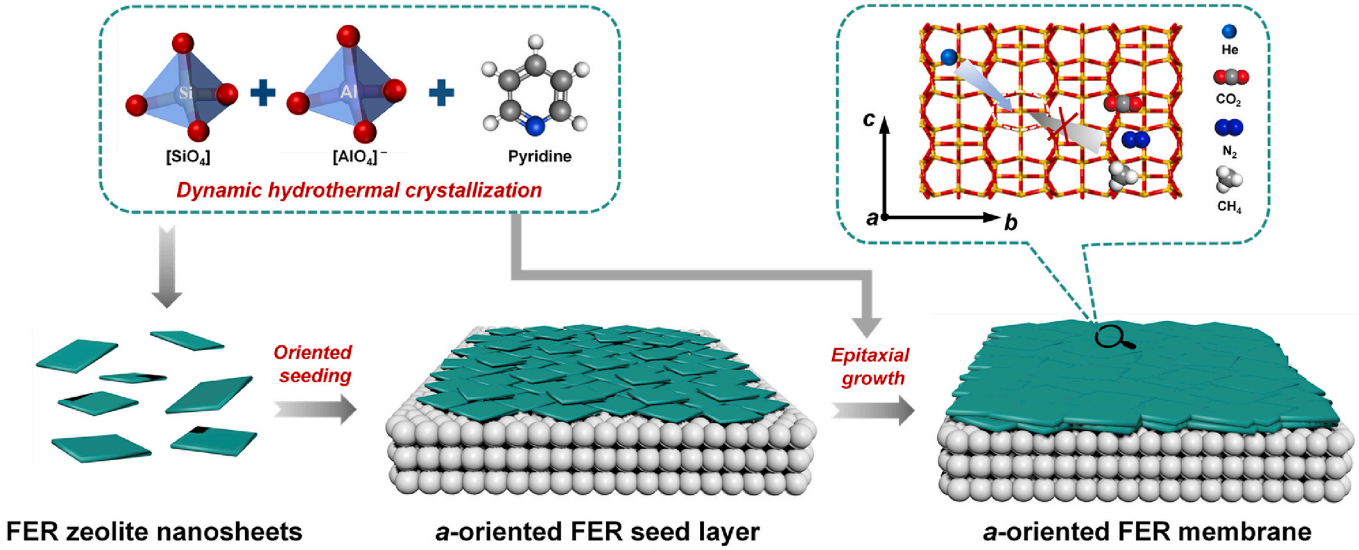

Fig. 1. Schematic illustration of the *a*-oriented FER membrane fabrication process.

the FER seed layer-desposited substrate was vertically placed in a 50 mL Teflon-lined autoclave, immersed in precursor solution, and put into a static convective oven. After hydrothermal reaction at 160 °C for 12 h, prepared FER zeolite membrane was thoroughly washed with copious of DI water, and air-dried in an oven at 90 °C overnight. Subsequently, obtained membrane was subjected to He permeation test for leak detection using the dead-end bubble flow meter method [28,29]. Membranes exhibiting negligible or very low He permeation (typically$<1 \times 10^{-10}$ mol/(m^2 s Pa) at 298 K and transmembrane pressure of 3 bar) are considered to be defect-free. The qualified membrane was finally calcined to remove organic templates trapped inside the zeolite pores.

2.5. Organic template removal

The template removal procedure was carried out as described in our previous study with slight modification [30–32]. The above membrane was vertically placed in a quartz tube and a dry oxygen containing 130 g/Nm^3 ozone (O_3/O_2) was introduced into the tube from the membrane side at a constant flow rate of 500 mL min^{-1}. The ozone was generated by an electrical discharge ozone generator (OSAN-CFG-O) and its concentration entering the unit was monitored using an ozone gas analyzer (UVOS-3300) purchased from OSAN Environmental and Technology (Dalian) Co., Ltd. The organic template occluded within the zeolitic pores was decomposed in an ozone environment at 250 °C for 72 h with a heating/cooling rate of 0.5 °C·min^{-1}.

2.6. Gas permeation test

The well-established Wicke-Kallenbach set-up was employed to measure the gas permeation performance of the O-ring sealed FER membranes (Fig. S5) [33,34]. For single-gas permeation test, the volumetric flow rate of each single gas (He, H_2, CO_2, N_2, CH_4) on the feed side was kept constant of 100 mL min^{-1}, and the permeated gas was removed from the permeate side by the sweep gas (Ar) with the same flow rate. Pressure differences in both sides were maintained at 1 bar, and operating temperature was kept at 180 °C. A calibrated gas chromatograph (7890B, Agilent) was employed to measure the concentration of single gas on the permeate side. The gas permeance of the permeated component i (P_i, mol m^{-2} s^{-1} Pa^{-1}) is defined as Equation (1):

$$P_i(\text{permeance}) = \frac{N_i}{A \times \Delta P_i} \tag{1}$$

$$1\ \text{GPU} = 3.348 \times 10^{-10}\ \text{mol}\cdot\text{m}^{-2}\cdot\text{s}^{-1}\cdot\text{Pa}^{-1}$$

where N_i (mol·s^{-1}) is the molar flow rate of the permeated component i, A (m^2) is the effective membrane area uncovered by O-ring, and ΔP_i (Pa) is the transmembrane partial pressure differences of the component i. The ideal selectivity ($S_{i/j}$) of different single component gases is defined as Equation (2):

$$S_{i/j} = \frac{P_i}{P_j} \tag{2}$$

where P_i (mol m^{-2} s^{-1} Pa^{-1}) and P_j (mol m^{-2} s^{-1} Pa^{-1}) denote the gas permeance of the permeated component i and j, respectively.

For mixed gas permeation test, the total volume flow rate of binary gas mixture (He/CO_2, He/N_2, and He/CH_4) on the feed side was kept constant of 100 mL min^{-1}, and the permeated gases were removed from the permeate side by the sweep gas (Ar) with a volumetric flow rate of 100 mL min^{-1}. For He/CH_4 separation tests, the feed temperature was varied from 30 to 180 °C under equimolar feed conditions. The long-term operating stability was conducted at 180 °C and 1 bar. The separation factor ($\alpha_{i/j}$) is defined as Equation (3):

$$\alpha_{i/j} = \frac{y_i / y_j}{x_i / x_j} \tag{3}$$

where y_i and y_j represent the molar fraction of component i and component j in the permeate side. x_i and x_j represent the molar fraction of component i and component j in the feed side. Single-gas and mixed-gas permeation data were obtained from at least triplicate measurements, where independent sample was tested for each measurement.

3. Results and discussion

3.1. Preparation of FER zeolite NSs

The first step involved dynamic hydrothermal crystallization of FER zeolite NSs. As shown in Fig. 2a and b, obtained powders exhibited monodispersed NS morphology with lateral size of 0.7–1.8 μm under optimized crystallization conditions (Fig. S6 and S7). TEM-EDXS mapping (Fig. S8) confirmed the homogeneous distribution of Si and Al elements throughout the NSs [35,36], yielding a Si/Al molar ratio (SAR) of 52.5, which was consistent with the nominal SAR of precursor solutions (Table S1). Simultaneously, relevant XRD diffraction peaks matched well with those of simulated FER phase, suggesting that obtained NSs indeed belonged to pure FER zeolite phase [37]. As confirmed by AFM results (Fig. 2c and d), the synthesized FER zeolite NSs exhibited a thickness of ~9.5 nm (equivalent to 5 unit cells of the FER structure), achieving an unprecedented aspect ratio (AR) of ~180, which represented the highest AR value reported to date for FER zeolites in the literature [37–40]. We further studied the textural properties of FER NSs. N_2 adsorption/desorption isotherm of FER NSs revealed typical type-I isotherm, indicating intrinsic microporous structure (Fig. 2e) [23]. Simultaneously, the BET surface area of FER NSs was calculated to be 255.6 m^2 g^{-1}, which was comparable to those previously reported for FER zeolites [39]. It should be emphasized that the use of dynamic crystallization was critical to achieving the well-defined NS morphology. For comparison, static oven was also employed for the crystallization process while keeping other reaction conditions unchanged. As illustrated in Fig. 2f and S9, the products appeared as irregular aggregates, predominantly composed of amorphous phase with negligible appearance of NS morphology. The distinct discrepancy in morphology and crystallinity was attributed to enhanced mass and heat transfer efficiency inherent to dynamic crystallization [34,41].

3.2. Deposition of oriented FER seed layer

Subsequently, vacuum-assisted hot-drop coating was employed for oriented deposition of NS seeds on the porous α-Al_2O_3 substrate (Fig. 3a). SEM results revealed that a uniform and densely-packed FER seed layer with thickness of ~170 nm was readily obtained under optimized conditions (Fig. 3b and c). The uniformity and high quality of this seed layer were critically dependent on the preparation of the coating suspension from a freeze-dried FER NS powder, which avoids the irreversible nanosheet aggregation caused by conventional thermal drying (Fig. S10). Corresponding XRD pattern confirmed the predominant *a*-orientation of the seed layer (Fig. 3f). For comparison, spin-coating was also evaluated for oriented deposition. Our results showed that spin-coating resulted in the formation of seed layer containing internal defects and misoriented NS seeds (Fig. S11). Therefore, adopting vacuum-assisted hot-drop coating was indispensable for achieving a seed layer with desired morphology. Inspired by the methodology presented by Agrawal et al. [42], we attempted to eliminate the interlayer gaps through direct heat treatment. However, dead-end He permeation tests indicated that nanoscale and interlayer gaps were not sealed (Table S2), rendering it unsuitable for gas separation. Consequently, epitaxial growth had become indispensable to seal non-selective

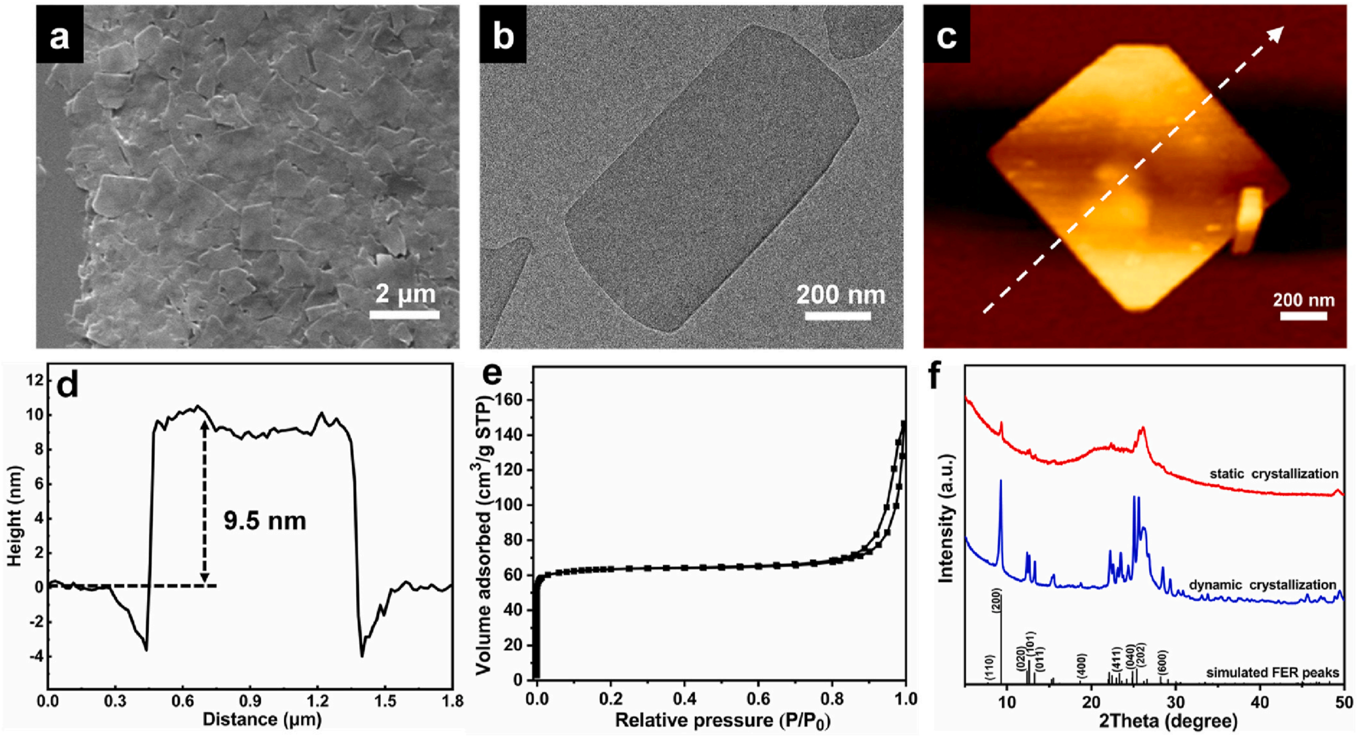

Fig. 2. (a) SEM image, (b) TEM image, (c) AFM surface image, (d) relevant line scan and (e) N_2 adsorption-desorption isotherm of FER zeolite NSs. (f) XRD patterns of FER zeolite NSs prepared by dynamic and static hydrothermal crystallization.

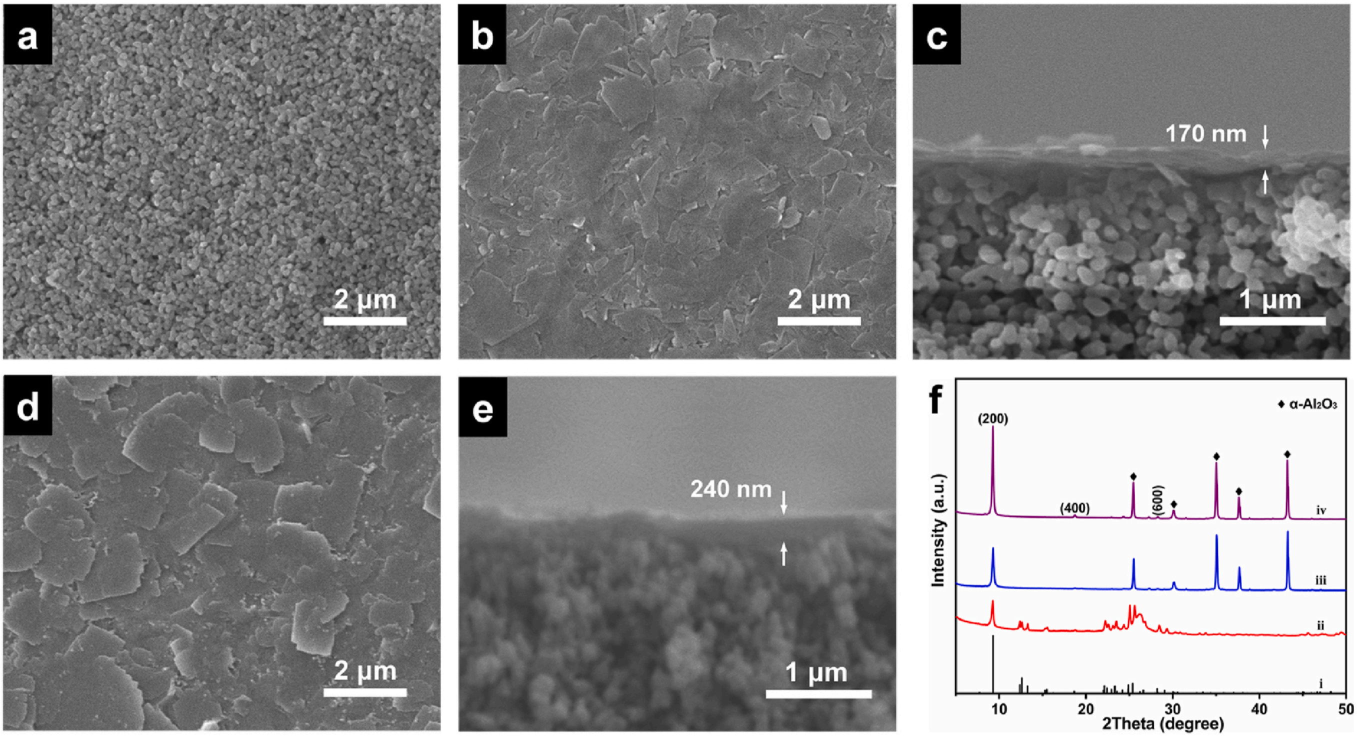

Fig. 3. SEM images of (a) porous α-Al_2O_3 substrate, (b, c) FER seed layer and (d, e) FER membrane after epitaxial growth at 160 °C for 12 h. (f) XRD patterns of (i) simulated FER peaks, (ii) FER zeolite NSs, (iii) FER seed layer and (iv) FER membrane.

interlayer defects in the seed layer.

3.3. Epitaxial growth of FER zeolite membrane

Herein, a precursor solution with composition identical to that of FER NSs was employed during the epitaxial growth process. Our results demonstrated that prolonging reaction duration facilitated complete sealing of interlayer defects (Fig. S12). After crystallization at 160 °C for 12 h, a well-intergrown and smooth membrane with the thickness of ~240 nm (Fig. 3d and e) was readily formed. Furthermore, relevant XRD pattern confirmed that resulting membrane was composed of pure FER zeolite phase with remarkable *a*-axis preferred orientation (Fig. 3f) [37]. To the best of our knowledge, this represented the first report on the fabrication of polycrystalline oriented FER membrane; moreover, its thickness was the thinnest among FER membranes reported in literature [43–45]. To better elucidate the twin suppression effect, precipitates that sedimented at the bottom of the reaction vessel after epitaxial growth were collected and characterized. XRD results indicated that they remained dominantly amorphous, demonstrating that undesired bulk nucleation rarely occurred during this process (Fig. S13) [31,46]. Even after extending the reaction duration to 24 h, the bulk nucleation could still be effectively inhibited (Fig. S14), enabling the formation of twin-free FER zeolite membrane (Fig. S15).

Preferred orientation of obtained FER zeolite membrane was further investigated using pole figure analysis. As shown in Fig. 4a, the pole figure of (200) plane displayed a symmetric peak with its maximum intensity at a tilt angle of 0°, indicating that the (200) plane in the membrane layer were primarily parallel to the support surface with no preferred in-plane orientation [47–50]. Quantitative analysis based on integrated peak intensity revealed that approximately 87 % of crystalline grains in the membrane were oriented with their *a*-axis within ±25° from normal to the membrane surface (Fig. 4b). Complementary evidence was obtained from the (411) pole figure presented in Fig. 4c. A distinct diffraction intensity maximum was observed at a tilt angle of 35° (Fig. 4c and d), which showed remarkable agreement with the theoretically predicted value of 35.48° assuming *a*-axis perpendicularity to the support surface [47]. All above observations were consistent with the (200) pole figure, verifying a high degree of *a*-out-of-plane orientation in the membrane. Simultaneously, mechanical stability of obtained FER membrane was evaluated through ultrasonic treatment. Relevant SEM image (Fig. S16a and b) indicated that not only the surface morphology of the treated FER membrane remained intact but also the XRD pattern (Fig. S16c) remained unchanged, implying a robust interaction between the membrane and the porous substrate.

3.4. *Gas permeation properties of FER zeolite membrane*

Finally, gas permeation behavior of the *a*-oriented ultrathin FER zeolite membrane was evaluated using the Wicke-Kallenbach technique. Our experimental results revealed a consistent decline in single gas permeance with increasing kinetic diameter of gas molecules with He displaying the highest average permeance (119.8 GPU) among the tested gases (Fig. 5a). Notably, average ideal selectivity of He/CO_2 (19.5) He/N_2 (23.8) and He/CH_4 (26.6) gas pairs significantly exceeded their respective Knudsen selectivity, confirming that few grain boundary defects existed in the membrane (Fig. 5b and Table S3) [51,52]. For an equimolar He/CH_4 mixture, our membrane exhibited an average SF of 24.5 with He permeance of 111.7 GPU (Table S4), which not only surpassed the 2008 upper bound for polymer membranes, but also well exceeded that of most inorganic molecular sieving membranes reported to date (Fig. S17 and Table S5). The superior He/CH_4 separation performance of prepared *a*-oriented FER zeolite membrane can be

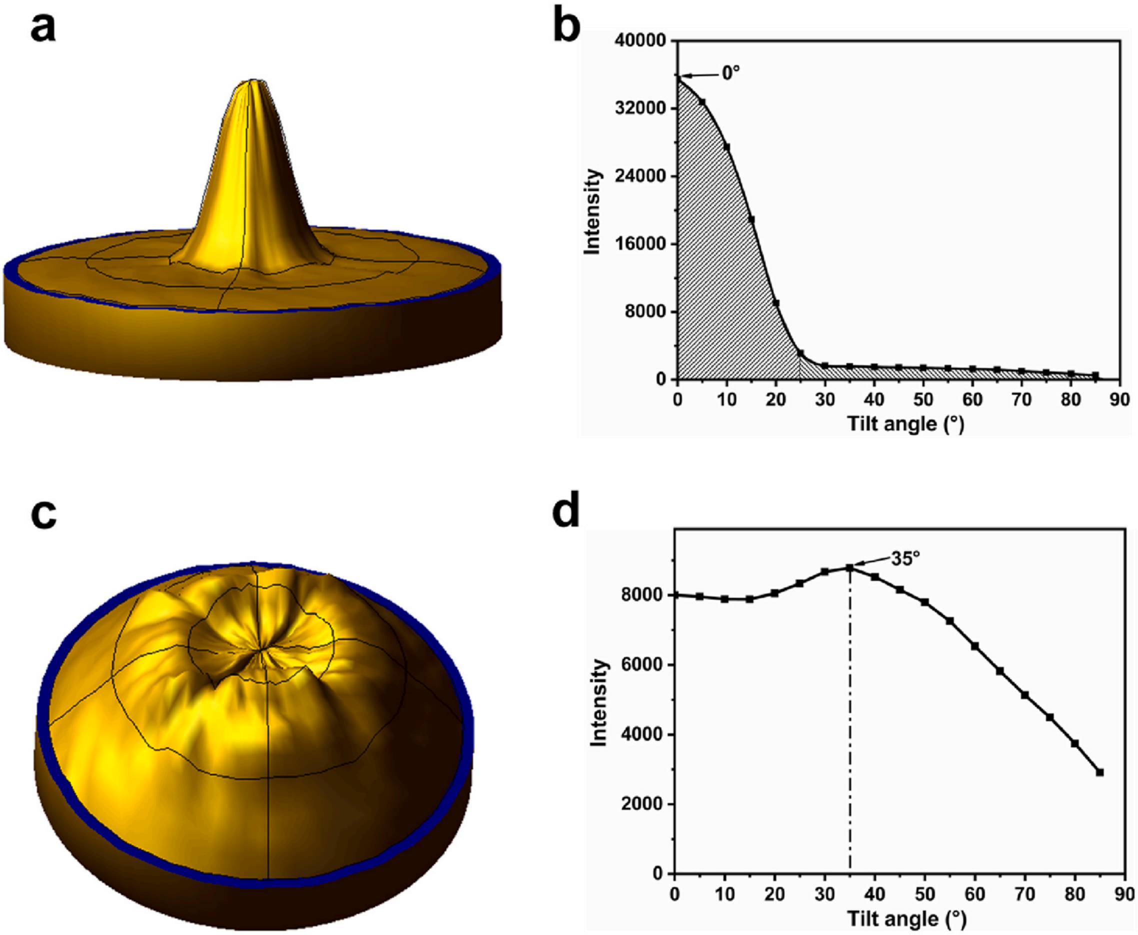

Fig. 4. Pole figures of (a, b) (200) plane and (c, d) (411) plane for *a*-oriented FER membrane after epitaxial growth at 160 °C for 12 h and the corresponding line plots of average intensity over the 360° rotation vs. tilt angle.

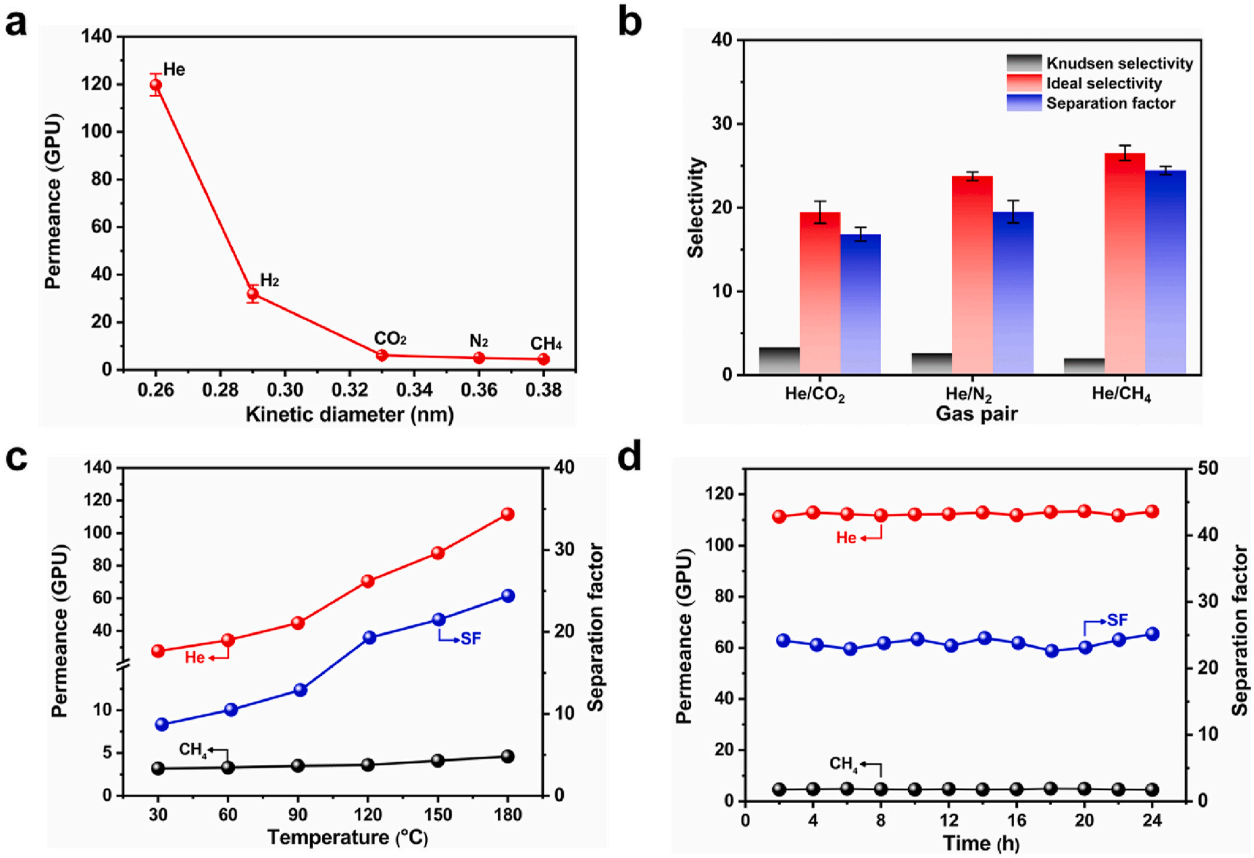

Fig. 5. (a) Single-gas permeation behavior of FER membrane measured at 180 °C and 1 bar. (b) Knudsen selectivity, ideal gas selectivity and separation factor of He over other gas molecules. (c) The dependence of equimolar He/CH_4 gas mixture separation performance of FER membrane on operating temperatures. (d) Stability test of FER zeolite membrane conducted at 180 °C and 1 bar toward equimolar He/CH_4 gas pair.

interpreted as follow: 1) the 0.28 nm-sized pore apertures along the *a*-axis, enabling precise molecular discrimination between He and CH_4 molecules, 2) the dominant *a*-orientation of the membrane layer, facilitating minimization of non-selective grain boundary defects. Furthermore, the influence of operation temperature on gas separation performance was investigated. As shown in Fig. 5c, both He permeance and SF of equimolar He/CH_4 mixture steadily increased as the operation temperature increased from 30 to 180 °C, which could be ascribed to a gradual pronounced size-sieving effect under elevated temperatures [53,54]. Moreover, both He permeance and SF of equimolar He/CH_4 mixture remained unchanged over continuous operation for 24 h (Fig. 5d), confirming a good durability of our FER membrane. Notably, for the separation of an equimolar He/CO_2 mixture, the membrane achieved a high separation factor of 16.8, which was superior to almost all zeolite membranes reported to date (Table S6). This excellent selectivity arises from the 0.28 nm pores precisely differentiating He from the larger CO_2 molecules, underscoring the distinct advantage of the *a*-oriented 6-MR pore structure for such challenging separations. While this proof-of-concept was performed on lab-scale supports, the fabrication approach herein holds significant promise for creating membranes on larger, industrially relevant configurations. Indeed, related methods based on the assembly of 2D building blocks have already proven effective for producing oriented crystalline membranes on commercial-type supports [55,56], demonstrating a viable pathway for module production.

4. Conclusions

In this study, we pioneered to prepare highly *a*-oriented ultrathin FER membranes via nanosheet-seeded epitaxial growth, marking the first successful fabrication of a polycrystalline oriented FER membrane. It was found that the introduction of high-aspect-ratio FER NSs as seeds and the effective inhibition of bulk nucleation during epitaxial growth were vital for guaranteeing the formation of the FER membrane with desired microstructure. Pole figure analysis quantatively verified the remarkable *a*-preferred orientation of the obtained membrane, with *a*-oriented grains accounting for up to 87 % of the membrane layer. Featuring vertically aligned 6-MR sieving channels and an ultrathin membrane layer, the membrane exhibited small-sized gas separation performance (e.g., He/CO_2, He/N_2, and He/CH_4) superior to state-of-the-art FER membranes, highlighting its potential for helium recovery from natural gas.

CRediT authorship contribution statement

Yi Liu: Writing – original draft, Validation, Methodology, Funding acquisition, Formal analysis, Data curation, Conceptualization. **Weili Qiang:** Validation, Formal analysis, Data curation. **Jinming Lu:** Investigation, Formal analysis. **Yi Liu:** Writing – review & editing, Supervision, Project administration, Funding acquisition, Conceptualization.

Declaration of competing interest

The authors declare that they have no known competing financial interests or personal relationships that could have appeared to influence the work reported in this paper.

Acknowledgements

The authors are grateful to the National Natural Science Foundation of China (22205030, 22408038, 22478056), Fundamental Research Fundamental Funds for the Central Universities (DUT24BS045, DUT22LAB602), National Key Research and Development Program of China (2023YFB3810700), the Postdoctoral Science Foundation of China (2022M710579, 2022TQ0051), Science Fund for Creative Research Groups of the National Natural Science Foundation of China (22021005), Liaoning Binhai Laboratory (LBLG-2024-07), State Key Laboratory of Catalysis (2024SKL-A-003), Science and Technology Innovation Fund of Dalian (2023JJ12GX024) for the financial support.

Appendix A. Supplementary data

Supplementary data to this article can be found online at https://doi.org/10.1016/j.memsci.2025.124437.

Data availability

Data will be made available on request.

References

[1] Y. Kong, X. Zhang, Q. Wang, Y. Liu, G. Liu, K. Wang, Enhancing helium separation by ionic-liquid-modulated nanoporous graphene oxide membrane, J. Membr. Sci. 722 (2025) 123861, https://doi.org/10.1016/j.memsci.2025.123861.

[2] K. Li, Q. Li, Z. Cai, Y. Weng, C. Ye, W. Ji, J. Li, B. Cheng, X. Ma, Microporosity effect of intrinsic microporous polyimide membranes on their helium enrichment performance after direct fluorination, J. Membr. Sci. 660 (2022) 120868, https://doi.org/10.1016/j.memsci.2022.120868.

[3] Z. Zhao, L. Ding, R. Hinterding, A. Mundstock, C. Belke, R.J. Haug, H. Wang, A. Feldhoff, MXene assisted preparation of well-intergrown ZIF-67 membrane for helium separation, J. Membr. Sci. 652 (2022) 120432, https://doi.org/10.1016/j.memsci.2022.120432.

[4] Z. Gao, Y. Sun, L. Bai, T. Li, J. Guan, F. Sun, F. Fan, G. He, C. Ma, Tuning fluorination of carbon molecular sieve membranes with enhanced reverse-selective hydrogen separation from helium, Small 21 (2025) e2411664, https://doi.org/10.1002/smll.202411664.

[5] C. Gong, X. Peng, M. Zhu, T. Zhou, L. You, S. Ren, X. Wang, X. Gu, Synthesis and performance of STT zeolite membranes for He/N_2 and He/CH_4 separation, Sep. Purif. Technol. 301 (2022) 121927, https://doi.org/10.1016/j.seppur.2022.121927.

[6] L. Liu, Q. Wu, S. Wang, W. Lai, P. Zheng, C. Wang, X. Wei, S. Luo, Highly selective and hydrocarbon-resistant polyimide hollow fiber membranes for helium recovery from natural gas, Ind. Eng. Chem. Res. 62 (2023) 708–716, https://doi.org/10.1021/acs.iecr.2c03907.

[7] Z. Li, X. Liu, Y. Sun, L. Gong, C. Liao, S. Luo, Pressure-resistant polyimide hollow fiber membranes for high-performance helium recovery from natural gas, Polymer 323 (2025) 128164, https://doi.org/10.1016/j.polymer.2025.128164.

[8] R. Weh, G. Xiao, E.S. Pouya, E.F. May, Direct helium recovery from natural gas by dual reflux pressure swing adsorption cascade, Chem. Eng. J. 450 (2022) 137894, https://doi.org/10.1016/j.cej.2022.137894.

[9] D. Li, M. Ye, C. Ma, N. Li, Z. Gu, Z. Qiao, Preparation of a self-supported zeolite glass composite membrane for CO_2/CH_4 separation, Smart Mol. 2 (2024) e20240009, https://doi.org/10.1002/smo.20240009.

[10] T. Xia, Y. Wu, T. Ji, W. Hu, K. Yu, X. He, B.H. Yin, Y. Liu, Mixed-matrix membranes incorporating hierarchical ZIF-8 towards enhanced CO_2/N_2 separation, Smart Mol. (2025) e20240066, https://doi.org/10.1002/smo.20240066.

[11] J. Ahn, W.-J. Chung, I. Pinnau, M.D. Guiver, Polysulfone/silica nanoparticle mixed-matrix membranes for gas separation, J. Membr. Sci. 314 (2008) 123–133, https://doi.org/10.1016/j.memsci.2008.01.031.

[12] Z. Kang, H. Guo, L. Fan, G. Yang, Y. Feng, D. Sun, S. Mintova, Scalable crystalline porous membranes: current state and perspectives, Chem. Soc. Rev. 50 (2021) 1913–1944, https://doi.org/10.1039/d0cs00786b.

[13] M. Carta, R. Malpass-Evans, M. Croad, Y. Rogan, J.C. Jansen, P. Bernardo, F. Bazzarelli, N.B. McKeown, An efficient polymer molecular sieve for membrane gas separations, Science 339 (2013) 303–307, https://doi.org/10.1126/science.1228032.

[14] J.G. Seong, W.H. Lee, J. Lee, S.Y. Lee, Y.S. Do, J.Y. Bae, S.J. Moon, C.H. Park, H. J. Jo, J.S. Kim, K.-R. Lee, W.-S. Hung, J.-Y. Lai, Y. Ren, C.J. Roos, R.P. Lively, Y. M. Lee, Microporous polymers with cascaded cavities for controlled transport of small gas molecules, Sci. Adv. 7 (2021) eabi9062, https://doi.org/10.1126/sciadv.abi9062.

[15] J.S. McHattie, W.J. Koros, D.R. Paul, Gas transport properties of polysulphones: 2. Effect of bisphenol connector groups, Polymer 32 (1991) 2618–2625, https://doi.org/10.1016/0032-3861(91)90343-H.

[16] M. Yavari, M. Fang, H. Nguyen, T.C. Merkel, H. Lin, Y. Okamoto, Dioxolane-based perfluoropolymers with superior membrane gas separation properties, Macromolecules 51 (2018) 2489–2497, https://doi.org/10.1021/acs.macromol.8b00273.

[17] Z. Dai, J. Deng, X. He, C.A. Scholes, X. Jiang, B. Wang, H. Guo, Y. Ma, L. Deng, Helium separation using membrane technology: recent advances and perspectives, Sep. Purif. Technol. 274 (2021) 119044, https://doi.org/10.1016/j.seppur.2021.119044.

[18] Y. Li, J. Yu, New stories of zeolite structures: their descriptions, determinations, predictions, and evaluations, Chem. Rev. 114 (2014) 7268–7316, https://doi.org/10.1021/cr500010r.

[19] Y. Li, J.H. Yu, Emerging applications of zeolites in catalysis, separation and host–guest assembly, Nat. Rev. Mater. 6 (2021) 1156–1174, https://doi.org/10.1038/s41578-021-00347-3.

[20] X. Han, W. Xu, F. Meng, Z. Liu, C. Liao, Recent advances in zeolite membranes for gas separation and pervaporation in petrochemicals, J. Mater. Chem. A 13 (2025) 10358–10387, https://doi.org/10.1039/d4ta08746a.

[21] R.B. Borade, A. Clearfield, Synthesis of ZSM-35 using trimethylcetylammonium hydroxide as a template, Zeolites 14 (1994) 458–461, https://doi.org/10.1016/0144-2449(94)90172-4.

[22] V.J. Margarit, M. Rocio Diaz-Rey, M. Teresa Navarro, C. Martinez, A. Corma, Direct synthesis of nano-ferrierite along the 10-Ring-Channel direction boosts their catalytic behavior, Angew. Chem. Int. Ed. 57 (2018) 3517–3521, https://doi.org/10.1002/anie.201711418.

[23] W. Dai, V. Ruaux, X. Deng, W. Tai, G. Wu, N. Guan, L. Li, V. Valtchev, Synthesis and catalytic application of nanorod-like FER-type zeolites, J. Mater. Chem. A 9 (2021) 24922–24931, https://doi.org/10.1039/d1ta06596c.

[24] E. Jang, J.H. Lee, S. Hong, Y. Jeong, J.C. Kim, D. Kim, H. Baik, E. Kim, N. Choi, J. Nam, S.J. Cho, S.K. Kwak, J. Choi, An unprecedented c-oriented DDR@MWW zeolite hybrid membrane: new insights into H_2-permselectivities via six membered-ring pores, J. Mater. Chem. A 8 (2020) 14071–14081, https://doi.org/10.1039/d0ta03892j.

[25] J.T. Crum, J.R. Crum, C. Taylor, W.F. Schneider, Characterization and analysis of ring topology of zeolite frameworks, Microporous Mesoporous Mater. 351 (2023) 112466, https://doi.org/10.1016/j.micromeso.2023.112466.

[26] Y. Liu, W.L. Qiang, T.T. Ji, M. Zhang, M.R. Li, J.M. Lu, Y. Liu, Uniform hierarchical MFI nanosheets prepared via anisotropic etching for solution-based sub–100-nm-thick oriented MFI layer fabrication, Sci. Adv. 6 (2020) eaay5993, https://doi.org/10.1126/sciadv.aay5993.

[27] S. Zhang, L. Shen, H. Deng, Q. Liu, X. You, J. Yuan, Z. Jiang, S. Zhang, Ultrathin membranes for separations: a new era driven by advanced nanotechnology, Adv. Mater. 45 (2022) e2108457, https://doi.org/10.1002/adma.202108457.

[28] H. Saulat, W. Feng, Z. Hu, M. He, J. Lu, Y. Zhang, J. Yang, C. He, Fabrication and characterization of polycrystalline MFI membranes on coarse macroporous supports for the separation of butane isomers, J. Membr. Sci. 727 (2025) 124065, https://doi.org/10.1016/j.memsci.2025.124065.

[29] T. Zhou, M. Zhu, Y. Dai, L. Chen, J. Xie, Y. Zhang, X. Wang, X. Gu, Static state synthesis of STT zeolite membranes for high-pressure H_2/CH_4 separation, J. Membr. Sci. 700 (2024) 122699, https://doi.org/10.1016/j.memsci.2024.122699.

[30] Y. Liu, M. Li, Z. Chen, Y. Cui, J. Lu, Y. Liu, Hierarchy control of MFI zeolite membrane towards superior butane isomer separation performance, Angew. Chem. Int. Ed. 60 (2021) 7659–7663, https://doi.org/10.1002/anie.202017087.

[31] Y. Liu, S. Chen, T. Ji, J. Yan, K. Ding, S. Meng, J. Lu, Y. Liu, Room-temperature synthesis of zeolite membranes toward optimized microstructure and enhanced butane Isomer separation performance, J. Am. Chem. Soc. 145 (2023) 7718–7723, https://doi.org/10.1021/jacs.3c00009.

[32] Y. Liu, S. Meng, X. Fan, K. Ding, J. Yan, M. Wu, S. Yang, J. Lu, Y. Liu, Mild fabrication of highly (*h0h*)-oriented MFI zeolite membrane from self-pillared nanosheets toward superior butane isomer and ammonia separation, Adv. Funct. Mater. 35 (2025) 2506949, https://doi.org/10.1002/adfm.202506949.

[33] S. Zhou, O. Shekhah, J. Jia, J. Czaban-Jóźwiak, P.M. Bhatt, A. Ramírez, J. Gascon, M. Eddaoudi, Electrochemical synthesis of continuous metal–organic framework membranes for separation of hydrocarbons, Nat. Energy 6 (2021) 882–891, https://doi.org/10.1038/s41560-021-00881-y.

[34] Y. Sun, J. Yan, Y. Gao, T. Ji, S. Chen, C. Wang, P. Lu, Y. Li, Y. Liu, Fabrication of highly oriented ultrathin zirconium metal-organic framework membrane from nanosheets towards unprecedented gas separation, Angew. Chem. Int. Ed. 62 (2023) e202216697, https://doi.org/10.1002/anie.202216697.

[35] W. Dai, C. Kouvatas, W.S. Tai, G.J. Wu, N.J. Guan, L.D. Li, V. Valtchev, Platelike MFI crystals with controlled crystal faces aspect ratio, J. Am. Chem. Soc. 143 (2021) 1993–2004, https://doi.org/10.1021/jacs.0c11784.

[36] J. Zhang, L. Ren, A. Zhou, W. Li, S. Shang, Y. Liu, Z. Jia, W. Liu, A. Zhang, X. Guo, C. Song, Tailored synthesis of ZSM-5 nanosheets with controllable *b*-Axis thickness and aspect ratio: strategy and growth mechanism, Chem. Mater. 34 (2022) 3217–3226, https://doi.org/10.1021/acs.chemmater.2c00001.

[37] H. Xu, W. Chen, G. Zhang, P. Wei, Q. Wu, L. Zhu, X. Meng, X. Li, J. Fei, S. Han, Q. Zhu, A. Zheng, Y. Ma, F.S. Xiao, Ultrathin nanosheets of aluminosilicate FER zeolites synthesized in the presence of a sole small organic ammonium, J. Mater. Chem. A 7 (2019) 16671–16676, https://doi.org/10.1039/c9ta04833b.

[38] X. Feng, P. Zhang, Y. Fang, W. Charusiri, J. Yao, X. Gao, Q. Wei, P. Reubroycharoen, T. Vitidsant, Y. Yoneyama, G. Yang, N. Tsubaki, Designing a hierarchical nanosheet ZSM-35 zeolite to realize more efficient ethanol synthesis from dimethyl ether and syngas, Catal. Today 343 (2020) 206–214, https://doi.org/10.1016/j.cattod.2019.02.054.

[39] H. Xu, Y. Yu, L. Zhu, C. Bian, H. Zhai, J. Tong, H. Wu, C. Shen, Preparation of aluminosilicate ferrierite zeolite nanosheets with controllable thickness in the presence of a sole organic structure directing agent, Molecules 25 (2020) 771, https://doi.org/10.3390/molecules25040771.

[40] H. Xu, J. Zhu, L. Zhu, E. Zhou, C. Shen, Advances in the synthesis of ferrierite zeolite, Molecules 25 (2020) 3722, https://doi.org/10.3390/molecules25163722.

[41] X. Li, Z. Wang, J. Zheng, S. Shao, Y. Wang, Y. Yan, Dynamic hydrothermal synthesis of a *b*-Oriented MFI zeolite film, Chin. J. Catal. 32 (2011) 217–223, https://doi.org/10.1016/s1872-2067(10)60167-2.

[42] M. Dakhchoune, L.F. Villalobos, R. Semino, L.M. Liu, M. Rezaei, P. Schouwink, C. E. Avalos, P. Baade, V. Wood, Y. Han, M. Ceriotti, K.V. Agrawal, Gas-sieving zeolitic membranes fabricated by condensation of precursor nanosheets, Nat. Mater. 20 (2021) 362–369, https://doi.org/10.1038/s41563-020-00822-2.

[43] C.J. Li, Y.J. Zhang, H. Chen, P.Y. He, High value-added utilization of silica fume to synthesize ZSM-35 zeolite membrane for Cd^{2+} removal, Mater. Lett. 260 (2020) 126940, https://doi.org/10.1016/j.matlet.2019.126940.

[44] N. Nishiyama, K. Ueyama, M. Matsukata, Synthesis of FER membrane on an alumina support and its separation properties, Prog. Zeolite Microporous Mater. 105 (1997) 2195–2202, https://doi.org/10.1016/S0167-2991(97)80690-8.

[45] N. Nishiyama, T. Matsufuji, K. Ueyama, M. Matsukata, FER membrane synthesized by a vapor-phase transport method: its structure and separation characteristics, Microporous Mater. 12 (1997) 293–303, https://doi.org/10.1016/S0927-6513(97)00076-X.

[46] Y. Liu, K.S. Ding, X. Fan, S.X. Chen, S.Y. Meng, J.H. Yan, Y.L. Gao, J.M. Lu, Y. Liu, Fabrication of highly *b*-oriented MFI zeolite film over broad temperature window, Chem. Eng. Sci. 293 (2024) 120076, https://doi.org/10.1016/j.ces.2024.120076.

[47] Z.P. Lai, M. Tsapatsis, J.R. Nicolich, Siliceous ZSM-5 membranes by secondary growth of *b*-oriented seed layers, Adv. Funct. Mater. 14 (2004) 716–729, https://doi.org/10.1002/adfm.200400040.

[48] X.D. Wang, B.Q. Zhang, X.F. Liu, Y.S. Lin, Synthesis of *b*-Oriented TS-1 films on chitosan-modified α-Al_2O_3 substrates, Adv. Mater. 18 (2006) 3261–3265, https://doi.org/10.1002/adma.200502772.

[49] Y. Liu, G. Zeng, Y. Pan, Z. Lai, Synthesis of highly *c*-oriented ZIF-69 membranes by secondary growth and their gas permeation properties, J. Membr. Sci. 379 (2011) 46–51, https://doi.org/10.1016/j.memsci.2011.05.041.

[50] M.C. Lovallo, A. Gouzinis, M. Tsapatsis, Synthesis and characterization of oriented MFI membranes prepared by secondary growth, AlChE J 44 (1998) 1903–1913, https://doi.org/10.1002/aic.690440820.

[51] T. Ji, L. Liu, M. Wu, K. Yu, X. He, Y. Liu, Subfreezing conversion of ALD-derived ZnO layer to ultra-thin ZIF-8 membrane for high-flux C_3H_6 production, Chem. Eng. Sci. 282 (2023) 119293, https://doi.org/10.1016/j.ces.2023.119293.

[52] A. Deng, X. Shen, Z. Wan, Y. Li, S. Pang, X. He, J. Caro, A. Huang, Elimination of grain boundary defects in zeolitic imidazolate framework ZIF-95 membrane via solvent-free secondary growth, Angew. Chem. Int. Ed. 60 (2021) 25463–25467, https://doi.org/10.1002/anie.202110828.

[53] Y. Song, Y. Sun, D. Du, M. Zhang, Y. Liu, L. Liu, T. Ji, G. He, Y. Liu, Fabrication of *c*-oriented ultrathin TCPP-derived 2D MOF membrane for precise molecular sieving, J. Membr. Sci. 634 (2021) 119393, https://doi.org/10.1016/j.memsci.2021.119393.

[54] T.T. Ji, Y.W. Sun, Y. Liu, M.R. Li, F. Wang, L.L. Liu, G.H. He, Y. Liu, Facile in situ hydrothermal synthesis of layered zirconium phenylphosphonate molecular sieve membranes with optimized microstructure and superb H_2/CO_2 selectivity, ACS Appl. Mater. Interfaces 12 (2020) 15320–15327, https://doi.org/10.1021/acsami.0c02789.

[55] B. Min, S.W. Yang, A. Korde, Y.H. Kwon, C.W. Jones, S. Nair, Continuous zeolite MFI membranes fabricated from 2D MFI nanosheets on ceramic hollow fibers, Angew. Chem. Int. Ed. 58 (2019) 8201–8205, https://doi.org/10.1002/anie.201903554.

[56] B. Wang, T. Wu, M. Yu, S. Li, R. Zhou, W. Xing, Highly ordered nanochannels in a nanosheet-directed thin zeolite nanofilm for precise and fast CO_2 separation, Small 16 (2020) e2002836, https://doi.org/10.1002/smll.202002836.